PNAS RESEARCH ARTICLE | ENGINEERING

Direct parallel electrosynthesis of high-value chemicals from atmospheric components on symmetry-breaking indium sites

Yuntong Sun[a], Liming Dai[b], Nicole L. D. Sui[a,c], Yinghao Li[a], Meng Tian[d,1], Jingjing Duan[b,1], Sheng Chen[b,1], and Jong-Min Lee[a,1]

Affiliations are included on p. 11.

Edited by Alexis Bell, University of California, Berkeley, CA; received May 14, 2024; accepted October 3, 2024

To tackle significant environmental and energy challenges from increased greenhouse gas emissions in the atmosphere, we propose a method that synergistically combines cost-efficient integrated systems with parallel catalysis to produce high-value chemicals from CO_2, NO, and other gases. We employed asymmetrically stretched InO_5S with symmetry-breaking indium sites as a highly efficient trifunctional catalysts for NO reduction, CO_2 reduction, and O_2 reduction. Mechanistic studies reveal that the symmetry-breaking at indium sites substantially improves d-band center interactions and adsorption of intermediates, thereby enhancing trifunctional catalytic activity. Employed in a flow electrolysis system, the catalyst achieves continuous and flexible production of NH_3, $HCOO^-$, and H_2O_2, maintaining over 90% Faradaic efficiency at industrial scales. Notably, the parallel electrolysis device reported in this study effectively produces high-value products like NH_4COOH directly from greenhouse gases in pure water, offering an economically efficient solution for small molecule synthesis and unique insights for the sustainable conversion of inexhaustible gases into valuable products. Therefore, this work possesses considerable potential for future practical applications in sustainable industrial processes.

CO_2 reduction reaction | N_2 reduction reaction | O_2 reduction reaction | symmetry-breaking | electrosynthesis

Significance

Electrocatalytic technologies powered by renewable energy have emerged as promising solutions for transforming harmful greenhouse gases like CO_2 and NO into useful chemicals. However, previous research has focused on converting single substrates into basic chemical products such as formate and ammonia, which require further processing into higher-value chemicals to meet the broad needs of society and the chemical industry. Herein, we report that InO_5S with symmetry-breaking indium sites acts as an efficient trifunctional catalyst for synthesizing formate, ammonia, and hydrogen peroxide and can directly convert greenhouse gases (CO_2 and NO) into ammonium formate using only pure water. This offers an economically efficient method for synthesizing high-value small molecules, presenting a significant advancement for sustainable chemistry.

Rampant combustion of fossil and biofuels over the decades has severely escalated emissions of greenhouse gases (e.g., CO_2 and NO_x) into the atmosphere, resulting in a detrimental impact on the environment and a burgeoning energy crisis (1–3). Electrocatalytic technologies, which leverage on renewable energy sources for driving electroconversion of earth-abundant inputs into value-added chemicals (e.g., electrochemical CO_2 reduction (CO_2RR), NO reduction (NORR), or O_2 reduction (ORR)), have thus emerged as sustainable and green solutions for mitigating our environmental predicament (4–7). However, previous electrocatalytic research has predominantly focused on converting single substrates into basic chemical products, such as formic acid (HCOOH, ~\$0.35 kg^{-1}), ammonia (NH_3, ~\$0.20 kg^{-1}) and hydrogen peroxide (H_2O_2, ~\$0.56 kg^{-1}) (6, 8, 9), which need to be further processed into higher-value chemical products to satisfy the broader needs of society and the chemical industry. In addition, their synthesis necessitates a variety of different catalysts, electrolytes, and experimental setups, leading to elevated production costs (Scheme 1*A* and *SI Appendix*, Note S1–S3) (10, 11).

Recently, to enhance the value of synthesized products, electrocatalytic C–N coupling reactions have emerged, converting CO_2 and nitrogenous pollutants into high-value downstream chemicals such as urea and methylamine (12–16). However, the practical application of electrocatalytic C–N coupling reactions is limited by several fundamental challenges. For instance, competitive side reactions, such as the propensity of multiple adsorbed species to undergo self-hydrogenation rather than the desired coupling reaction as well as hydrogen evolution reaction (HER), collectively result in lower Faradaic efficiencies (FE), reduced current densities, and the formation of complex product mixtures (16, 17).

An effective strategy for optimizing C–N coupling reactions is to first synthesize the primary products within the same device and then flexibly convert them into the desired complex downstream chemicals, such as ammonium formate (~\$2.52 kg^{-1}, approximately an order of magnitude higher in value than the primary products, *SI Appendix*, Note S1) through physical or chemical methods. This approach has three major advantages (Scheme 1*B*): 1) achieving industrial-scale current densities, exceeding 90% FE and remarkable selectivity; 2) integrating different reactions within a single electrolysis device,

This article is a PNAS Direct Submission.

[1]To whom correspondence may be addressed. Email: tianmeng@njust.edu.cn, jingjing.duan@njust.edu.cn, sheng.chen@njust.edu.cn, or jmlee@ntu.edu.sg.

This article contains supporting information online at https://www.pnas.org/lookup/suppl/doi:10.1073/pnas.2409620121/-/DCSupplemental.

Published November 15, 2024.

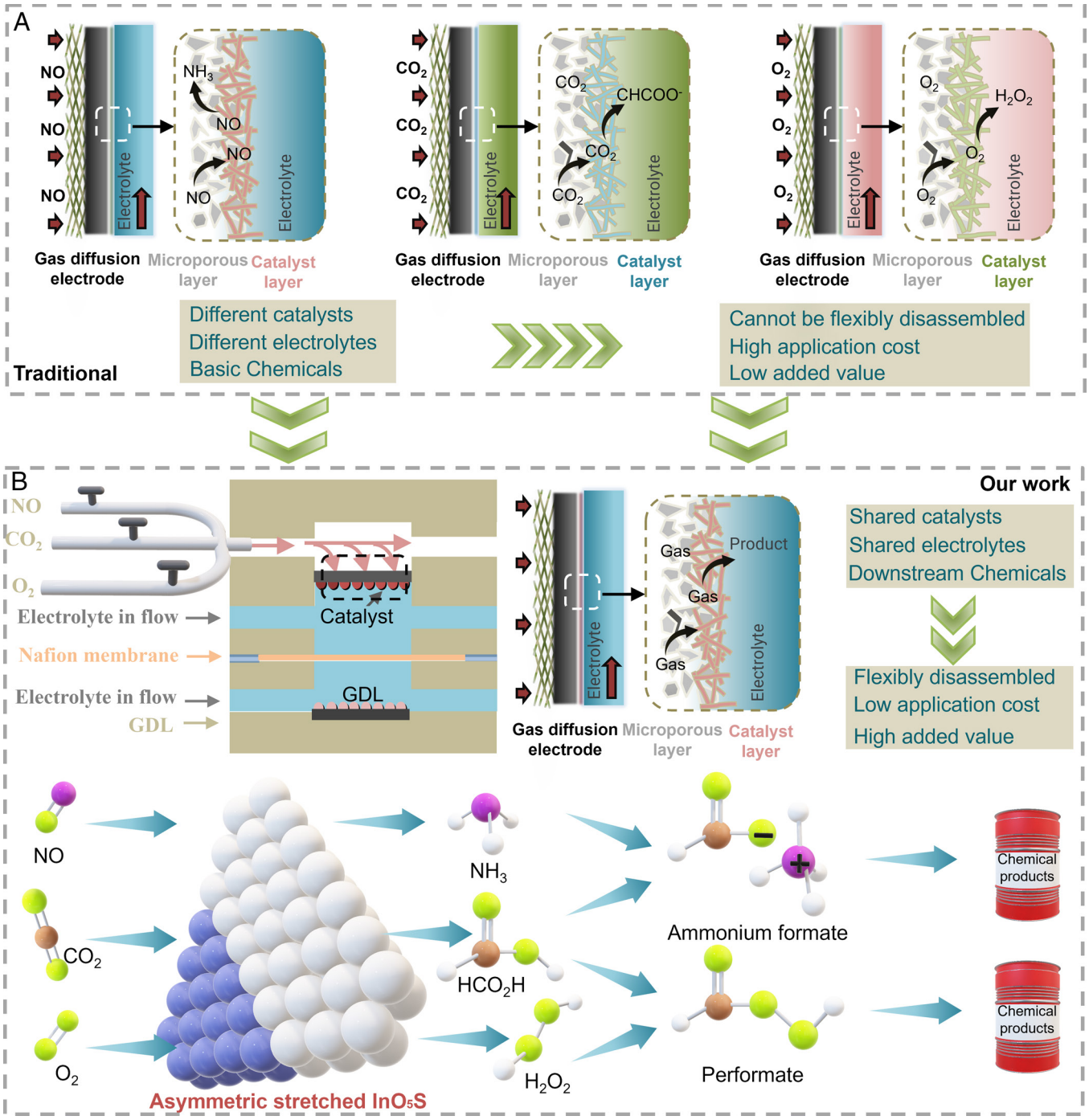

Scheme 1. Schematic illustration of the design strategy for synthesizing small molecules (NH_3, $HCOO^-$, and H_2O_2) from air and parallel catalysis electrosynthesis of high-value-added products with an asymmetrically stretched InO_5S as a trifunctional cathode catalyst. (*A*) Schematic illustrating the traditional process of electrocatalytic synthesis of small molecules (NH_3, $HCOO^-$, and H_2O_2). Different catalysts and electrolytes are required to synthesize different small molecules through traditional electrocatalytic processes, resulting in low flexibility and high application costs. (*B*) The process of integrating electrocatalytic synthesis of small molecules and hand-over to synthesize high-value-added products. Using the same catalytic solution to flexibly synthesize small molecules in the same electrolyte reduces application costs. The small molecules produced can be mixed on demand to form high-value-added products.

avoiding the use of multiple catalysts and complex electrolytes, and enabling flexible switching of products without disassembling the device, thereby reducing production costs; and 3) producing a wide array of downstream chemical products from various primary products, leading to enhanced product value. Despite the many advantages of this technique, current catalysts are primarily designed for single catalytic reactions (18–20). Multifunctional electrocatalysts, with their multiple active sites, can simultaneously catalyze two or more distinct electrochemical reactions (21). As emphasized by Prof. Sagi and Pillai, these catalysts are essential for addressing urgent energy challenges and are crucial for the development of sustainable energy systems (21). Therefore, there is a pressing need to develop catalysts with multifunctional active sites to achieve efficient catalysis.

Indium (In)-based catalysts exhibit high oxophilicity (22). The partially oxidized surface layer can effectively suppress HER and thermodynamically favor the adsorption of oxygen-containing intermediates, such as *OCHO, for enhanced formate selectivity (22). Therefore, In-based catalysts inherently hold promise as multifunctional catalysts, exhibiting excellent catalytic activity and

selectivity in CO_2RR to $HCOO^-$ (22), NORR to NH_3 (23), and ORR to H_2O_2 (24). Symmetry-breaking, which refers to the disruption of the original balance or symmetry of a material or central atom structure, is an effective strategy for precisely tuning the electronic structure of catalytic sites (25–27). By breaking inherent symmetry, active sites with unique electronic configurations can be created, enhancing the adsorption and desorption of intermediates (25–27). Integrating symmetry-breaking strategies into In-based catalysts can alter the electronic structure of In sites at the atomic level, steering the catalyst toward electronic configurations more favorable for the adsorption of intermediates and desorption of products, thereby further optimizing the multifunctional catalytic ability.

Herein, asymmetrically stretched InO_5S with symmetry-breaking In sites was designed, serving as a highly selective and active trifunctional catalyst for CO_2RR, NORR, and ORR. The trifunctional catalytic activity and enhancement mechanism of the symmetry-breaking In sites were elucidated through density functional theory (DFT) calculations and in situ experiments. Additionally, when the catalyst was integrated into a flow electrolysis system, findings reveal a continuous and versatile production of NH_3, $HCOO^-$, and H_2O_2, which consistently exceeds 90% in average FE. Furthermore, in the specially designed parallel electrolysis device, high-value chemical products, such as NH_4COOH, were efficiently synthesized from greenhouse gases like NO and CO_2 in pure water. This work represents a significant advancement in converting greenhouse gases into high-value downstream chemical products, unveiling significant potential for future applications in sustainable industrial processes.

Results

Synthesis and Structural Characterizations. Asymmetrically stretched InO_5S with symmetry-breaking In sites was synthesized through a two step procedure, involving a hydrothermal treatment to first obtain an indium metal-organic framework (In-MOF) nanorod precursor containing sulfur (S), followed by annealing in the absence of any additional S sources (*SI Appendix*, Fig. S1). Symmetrically stretched InO_6 and InS_6 were also prepared via a similar procedure (Information under Material Synthesis). X-ray diffraction (XRD) patterns of the as-synthesized asymmetrically stretched InO_5S reveal well-crystallized diffraction peaks assigned to the planes of In_2O_3 (space group *Ia-3*, JCPDS No. 71-2195, a = b = c = 10.117 Å) and In_2S_3 (space group *Fd-3 m*, JCPDS No. 84-1385, a = b = c = 10.774 Å) (*SI Appendix*, Figs. S2–S4). Scanning electron microscopy (SEM) images reveal uniform nanorod structures of InO_5S with a size profile corresponding to a few micrometers in length and a diameter of ~100 nm, inherited from the morphology of fabricated In-MOF (*SI Appendix*, Figs. S5–S7). The corresponding element mapping proves that In, O, and/or S are homogenously distributed across the nanorods (*SI Appendix*, Figs. S5–S7 and Table S5).

High-angle annular dark field-scanning transmission electron microscopy images (HAADF-STEM, *SI Appendix*, Fig. S8), corresponding fast Fourier transformation (FFT) patterns, and intensity line scans show that InO_5S possesses distinct In_2O_3 and In_2S_3 domains, with well-resolved lattice fringes and interplanar distances of 0.326 and 0.41 nm, which match well with the (311) plane of In_2S_3 and the (211) plane of In_2O_3, respectively. Furthermore, the magnified HAADF-STEM (Fig. 1*A*) image and corresponding molecular model of InO_5S (inset of Fig. 1*A*) show obvious atomic dislocation and lattice distortions resulting from strain at the phase interface, as verified by geometric phase analysis (GPA) (Fig. 1*B*). In comparison, HAADF-STEM, diffraction analysis, and GPA of both InO_6 and InS_6 (*SI Appendix*, Figs. S9-S16) showed uniform interatomic spacings without atomic dislocations, lattice distortions, and strain, indicating that the crystal structures of InO_6 and InS_6 possess good symmetry.

X-ray absorption near-edge structure (XANES) and extended X-ray absorption fine structure (EXAFS) spectroscopy were conducted, to elucidate insight into the fine coordination structures of InO_5S. As shown in Fig. 1*C*, the In K-edge energy position gradually increases from InS_6 through InO_5S to InO_5, moving away from In foil. Similarly, the valence state, determined via the functional relationship between ΔE and the oxidation states, increases from InS_6, InO_5S, to InO_5 which were +2.43, +2.75, and +3, respectively (Fig. 1*E*). Fourier-transform k^3-weighted EXAFS (FT-EXAFS) spectra reveal distinct peaks at ~2.2 Å and 3.3 Å (Fig. 1*D*), corresponding to the In–O/In–S and In–In scattering paths. Moreover, EXAFS spectra fitting reveals that the In–O bond length in InO_5S is slightly longer than InO_6 (2.24 vs. 2.16 Å), whereas the In–S bond length in InO_5S is marginally shorter than in InS_6 (2.33 vs. 2.4 Å, *SI Appendix*, Table S6). Additionally, the EXAFS fitting results indicate that InO_5S has an In–O coordination number (CN) of ~5 at ~2.24 Å and an In–S coordination number of ~1 at ~2.33 Å (*SI Appendix*, Figs. S17–S20), suggesting that In is coordinated with five O atoms and one S atom to form asymmetrically stretched InO_5S. The wavelet transform analysis results are consistent and further support the EXAFS fitting results (*SI Appendix*, Fig. S21).

Subsequently, DFT calculations were performed to reveal the redistribution of atomic-level electronic structure at the In site resulting from asymmetric stretching. The calculated density of states (DOS, Fig. 1 *F–H*) and band structure (*SI Appendix*, Fig. S22) show that InO_5S and InO_6 exhibit semiconductive behavior, while InS_6 presents metallic conductivity for the In and S orbitals across the Fermi level (E_f). Compared to InO_6, InO_5S with its smaller band gap (0.2 eV) and more electrons near E_f, exhibits better electronic conductivity, beneficial for rapid electron transfer processes, thereby facilitating enhanced catalytic activity. As shown in Fig. 1*I*, the work function of InS_6 is 5.25 eV, which is significantly lower than the 5.93 eV of InO_6, suggesting the tendency for electron transfer from the S–In side to the In–O side in InO_5S (*SI Appendix*, Fig. S23). Charge density difference calculations further verify a transfer of 2.15 electrons from the S–In side to the In–O side of InO_5S (Fig. 1*J*), leading to electron dissipation on the S–In side and electron accumulation on the In–O side (*SI Appendix*, Fig. S24), thereby forming an internal electric field. Moreover, calculations of the electron localization function (ELF, Fig. 1*K*) indicate that the internal electric field is induced via formation of symmetry-breaking structure. The relationship between the internal electric field and the d-band center was also examined, showing that as the electric field increased from 0.01 V $Å^{-1}$ to 0.07 V $Å^{-1}$, a gradient increase in the d-band center values was observed (Fig. 1*L*), indicating that an appropriate electric field can elevate the d-band center, which can enhance catalytic performance.

Electrocatalytic NORR Performance and Mechanism. The electrochemical NORR performance of asymmetrically stretched InO_5S was evaluated in a 0.1 M NO-saturated Na_2SO_4 electrolyte (without *iR*-compensation). The linear sweep voltammetry (LSV, Fig. 2*A*) curves demonstrate a substantially higher current density for InO_5S under NO-saturated conditions compared to Ar-saturated conditions, indicating an effective activation of NO by InO_5S. Quantitative studies on the NORR of InO_5S were conducted, revealing a gradual increase in NH_3 yield rates with a negative shift of potential, reaching a

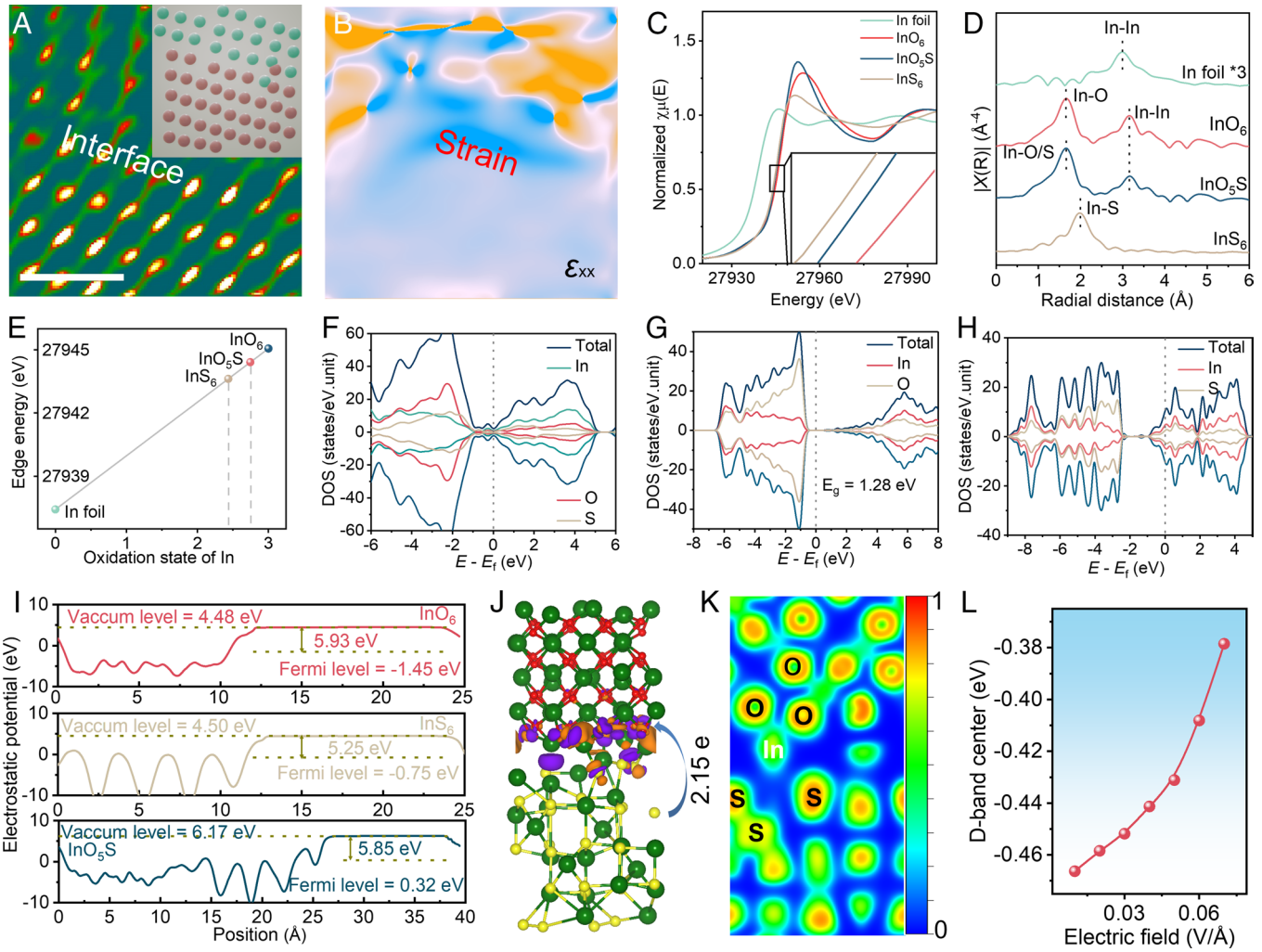

Fig. 1. Atomic-scale crystal and electronic structural characterizations of the asymmetrically stretched InO_5S. (*A*) HAADF-TEM image (Scale bar, 1 nm); the inset of (*A*) displays the corresponding structural model, showing only In atoms. (*B*) Strain field map from GPA for axial strain (ε_{xx}). (*C*) In K-edge XANES spectra of InO_5S, InO_6, InS_6, and In foil; the inset of (*C*) shows the enlarged near-edge pattern. (*D*) Fourier transform of the EXAFS spectra for InO_5S, InO_6, InS_6, and In foil. (*E*) Relationship between In K-edge threshold value (E_0) and oxidation state. DOS profiles of (*F*) InO_5S, (*G*) InO_6, and (*H*) InS_6. (*I*) Calculated work function for InO_5S, InO_6, and InS_6. (*J*) The charge density difference and (*K*) the ELF of the InO_5S. (*L*) Relationship between the d-band center and the electric field.

maximum NH_3 yield rate of 163.76 μmoL h^{-1} cm^{-2} at −0.8 V (vs. RHE, Fig. 2*B*). Moreover, InO_5S maintains an exceptionally high FE of over 90% across a wide potential range of 0.5 V, particularly achieving a maximum FE of 96.94% at −0.6 V (vs. RHE, Fig. 2*C*). This indicates that InO_5S possesses excellent NH_3 production capability and selectivity, comparable to the NORR activity of previously reported catalysts (*SI Appendix*, Table S7). This result was further confirmed via a series of control experiments (*SI Appendix*, Fig. S25), including InO_5S in 0.1 M Ar saturated Na_2SO_4 electrolyte at −0.8 V (vs. RHE, 2.31 μmoL h^{-1} cm^{-2}), blank CC at −0.8 V (vs. RHE, 6.75 μmoL h^{-1} cm^{-2}), and InO_5S under open circuit potential (OCP, 0.76 μmoL h^{-1} cm^{-2}), confirming that the NH_3 production originated from NO rather than external contamination. Notably, the activity of InO_5S (163.76 μmoL h^{-1} cm^{-2} and 96.94%, *SI Appendix*, Fig. S25) was far superior compared to InO_6 (131.69 μmoL h^{-1} cm^{-2} and 84.29%) and InS_6 (102.25 μmoL h^{-1} cm^{-2} and 65.64%). Although all samples exhibited similar steady-state current densities (*SI Appendix*, Fig. S26), InO_5S has the highest partial current density for NH_3 production throughout the entire test range (*SI Appendix*, Fig. S27), indicating that asymmetrically stretched InO_5S can most effectively inhibit HER side reactions, leading to its superior NORR activity.

To probe insight into the origin of the remarkable NORR activity of InO_5S, DFT calculations were performed. For symmetrical In sites present in InO_6 and InS_6 (*SI Appendix*, Figs. S28 and S29), the conversion from *NO to *NHO (initial hydrogenation) was found to be the rate-determining step (RDS), with corresponding energy barriers of 0.54 eV and 0.73 eV (Fig. 2*D*), respectively. Conversely, the symmetry-breaking In sites in InO_5S successfully transform the uphill barrier of the initial hydrogenation into a spontaneous process, thereby changing the RDS to *NHO → *NHOH (Fig. 2*D*), with a corresponding barrier of only 0.37 eV. This indicates that symmetry-breaking In sites favor NORR activity by altering the RDS. Based on the integrated crystal orbital Hamilton population (-ICOHP, Fig. 2*E*) results, the In–N bond in *ON-InO_5S exhibits an optimal bond strength (1.62 eV), which is significantly lower than InO_6 and InS_6, indicating appropriate adsorption of NO on the catalyst surface. Additionally, the smallest N–O bond strength of NO on InO_5S is 18.42 eV, suggesting that NO is more easily polarized on InO_5S. This is corroborated by the smaller overlap of projected density of states (*SI Appendix*, Fig. S30) for N and O orbitals on InO_5S compared to InS_6 and InO_6. Furthermore, a crystal orbital Hamilton population (COHP, Fig. 2 *F* and *G*) study on the bonding-antibonding characteristics of the In–N and N–O bonds at the In site reveals

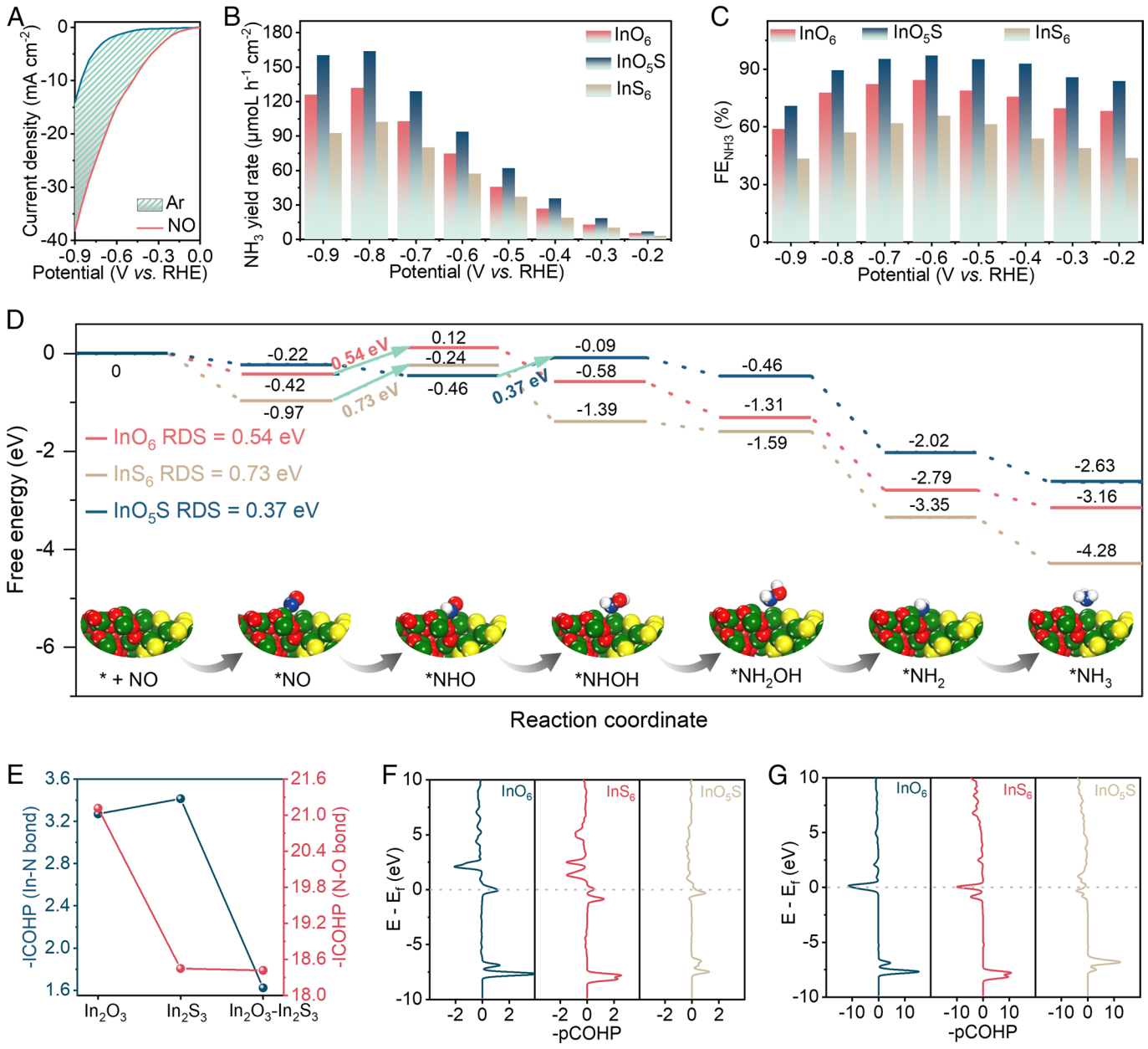

Fig. 2. Electrochemical NORR performance of asymmetrically stretched InO_5S. (*A*) LSV curves in NO- and Ar-saturated 0.1 M Na_2SO_4 solutions. (*B* and *C*) NH_3 yield rates and FEs at different applied potentials. (*D*) Calculated free energy diagrams for NORR on InO_5S, InO_6, and InS_6 with the schematic of the NORR reaction pathway on InO_5S. (*E*) Strength of the In–N and N–O bond as elucidated by the integrated-COHP (–ICOHP). COHP for (*F*) In–N and (*G*) N–O.

that fewer bonding orbitals occupied on InO_5S contribute to the formation of an appropriate In–N bond and weakening of the N–O bond compared to InO_6 and InS_6. The weakening of the N–O bond serves crucial in facilitating subsequent hydrogenation steps, lowering the barrier and thus enhancing the reaction kinetics of NORR. Therefore, the symmetry-breaking In sites on asymmetrically stretched InO_5S can moderately adsorb NO and significantly polarize the N–O bond, promoting subsequent hydrogenation steps for NH_3 production.

Electrocatalytic CO_2RR Performance and Mechanism. The electrochemical CO_2RR performance of asymmetrically stretched InO_5S was evaluated. As evident from the LSV curves, InO_5S exhibits significantly higher current densities under CO_2-saturated electrolyte compared to Ar-saturated electrolyte, indicating superior CO_2RR activity and selectivity of InO_5S over InO_6 and InS_6 (Fig. 3*A* and *SI Appendix*, Fig. S31). Moreover, InO_5S (Fig. 3*B*) displayed exceptional $HCOO^-$ production FE ($FE_{formate}$) exceeding 90% over a wide potential range of 1.0 V, with a maximum $FE_{formate}$ of 95.18% achieved at −1.0 V (vs. RHE), surpassing the $FE_{formate}$ of InO_6 (89.53% at −0.4 V vs. RHE, *SI Appendix*, Fig. S32) and InS_6 (76.73% at −0.8 V vs. RHE, *SI Appendix*, Fig. S33). The $HCOO^-$ production rate increases gradually with potential, reaching a maximum of 7.58 mmoL h^{-1} cm^{-2} at −2.0 V (vs. RHE), significantly higher than that of InO_6 (4.15 mmoL h^{-1} cm^{-2}) and InS_6 (2.20 mmoL h^{-1} cm^{-2}, *SI Appendix*, Fig. S34).

Notably, InO_5S consistently demonstrates higher $FE_{formate}$ (Fig. 3*C*) and lower FE_{CO} and FE_{H2} (*SI Appendix*, Fig. S35) compared to InO_6 and InS_6 throughout the entire potential range. Specifically, at −1.0 V (vs. RHE), the formate partial current density ($j_{formate}$) on InO_5S (Fig. 3*D*) reached as high as 107.22 mA cm^{-2}, outperforming that of InO_6 and InS_6 by 1.72 and 2.56 folds, respectively. In addition, InO_5S achieved the highest $j_{formate}$ of

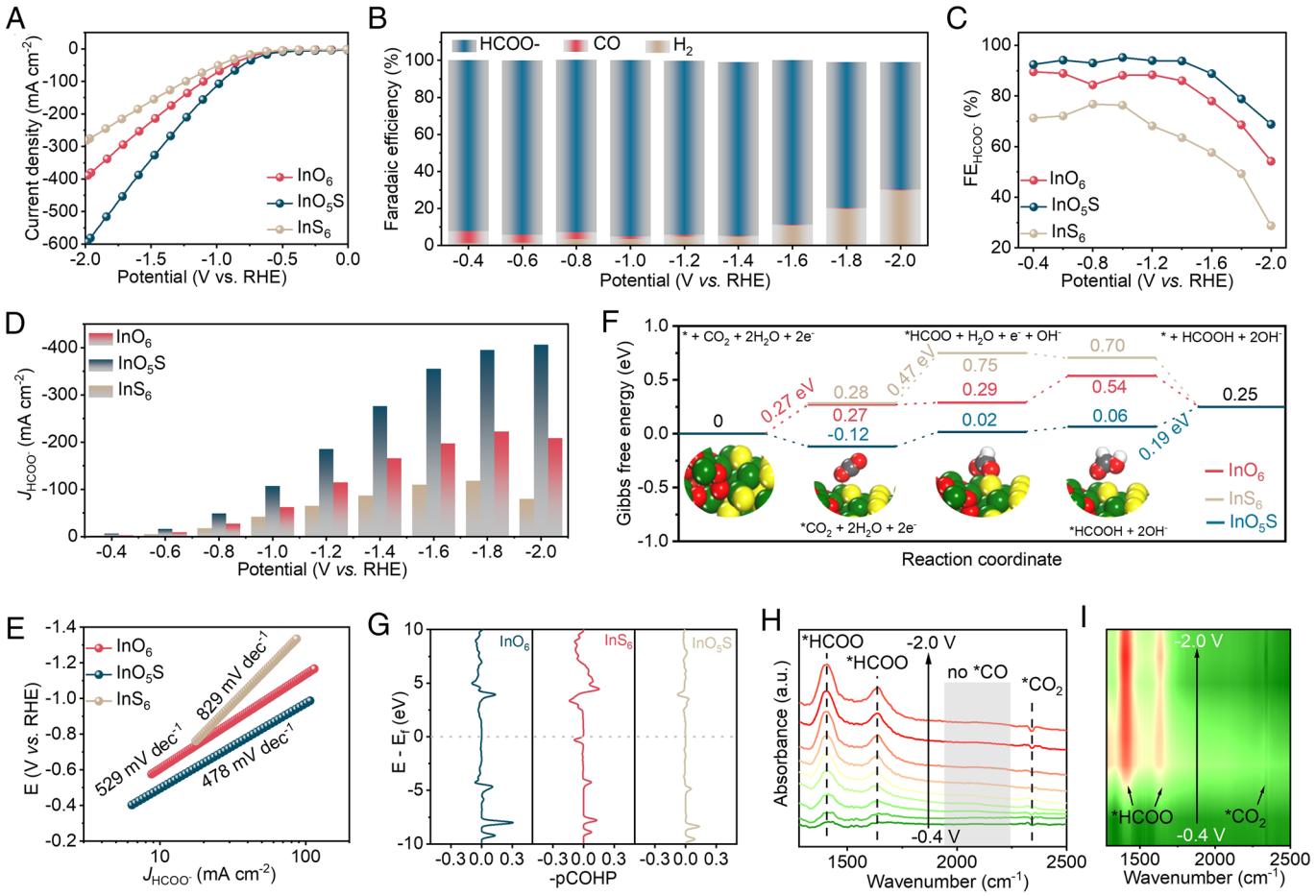

Fig. 3. Electrochemical CO_2RR performance of asymmetrically stretched InO_5S. (*A*) LSV curves in CO_2-saturated 0.1 M Na_2SO_4 solutions. (*B*) FEs of $HCOO^-$, CO, and H_2 at different applied potentials. Comparison of FEs_{HCOO^-} (*C*), j_{HCOO^-} (*D*), and Tafel plots (*E*) for InO_5S, InO_6, and InS_6. (*F*) Calculated free energy diagrams for CO_2RR on InO_5S, InO_6, and InS_6 with the schematic of the CO_2RR reaction pathway on InO_5S. (*G*) COHP for In–O. Electrochemical in situ FT-IR spectra (*H*) and corresponding contour plots (*I*) for InO_5S.

406.42 mA cm^{-2}, surpassing the values obtained for InO_6 (222.53 mA cm^{-2}) and InS_6 (117.92 mA cm^{-2}). This superior performance was further validated by partial Tafel slope (Fig. 3*E*) and cathodic energy efficiency (CEE) analysis for formate production (*SI Appendix*, Figs. S36 and S37). Additionally, InO_5S exhibits enhanced CO_2RR activity and selectivity by effectively suppressing undesired H_2 and CO evolution, as shown by its consistently lower partial current densities for CO and H_2 production than InO_6 and InS_6 (*SI Appendix*, Figs. S38 and S39). The excellent activity and selectivity of InO_5S contribute to it being among the best catalysts for CO_2RR to formate reported thus far (*SI Appendix*, Fig. S40 and Table S8).

DFT calculations were performed to elucidate the mechanism of efficient CO_2RR on InO_5S. As shown in Fig. 3*F*, the RDS for formate production during CO_2RR on InO_5S was found to be only 0.19 eV, which is significantly lower than both InO_6 (0.27 eV, *SI Appendix*, Fig. S41) and InS_6 (0.47 eV, *SI Appendix*, Fig. S42). This remarkable difference promotes a seamless formate production process with improved reaction kinetics. Furthermore, COHP calculations were performed to analyze the chemical bonding and antibonding interactions of CO_2 at the In sites (Fig. 3*G*). The COHP results of InO_5S revealed that bonding interactions between In–O exist in the valence states (below E_f), while In–O antibonding states were predominant in the conduction band (above E_f), indicating the stability in bonding configuration. Conversely, antibonding states were observed in valence states of both InO_6 and InS_6 (Fig. 3*G*), leading to a weakened bond strength between In and O, consistent with CO_2 adsorption calculations (Fig. 3*F*). Besides, PDOS calculations demonstrated higher concentrations of O orbitals and increased overlap between O and In orbitals for CO_2 adsorbed on InO_5S, further validating the enhanced adsorption capabilities of CO_2 on symmetry-breaking In sites (*SI Appendix*, Fig. S43).

In situ attenuated total reflection Fourier-transform infrared spectroscopy (ATR-FTIR) revealed a distinct chemical adsorption peak for CO_2 at ~2,340 cm^{-1} on InO_5S at all applied potentials (Fig. 3 *H* and *I*), indicating the pronounced adsorption affinity of CO_2 on InO_5S. The vibrational bands located at ~1,400 and 1,636 cm^{-1}, which can be attributed to the stretching vibrations of adsorbed HCOO* intermediates (Fig. 3 *H* and *I*), exhibit a significant increase in peak area with negative shifts in potential, thereby affirming the dominant presence of HCOO* intermediates on the InO_5S surface. Moreover, no stretching vibrations of COOH* were detected at 1,573 cm^{-1}, suggesting that formate is produced predominantly from HCOO* rather than COOH*. Also, no significant adsorption of *CO by-products was observed on the InO_5S surface within the range from ~2,000 to ~2,160 cm^{-1} (Fig. 3 *H* and *I*). Taken collectives, these findings affirm the outstanding activity and selectivity of InO_5S for CO_2RR toward formate production, in agreement with both the experimental findings and DFT calculations.

Electrocatalytic ORR Performance and Mechanism. Finally, the electrochemical 2e ORR performance of InO_5S was evaluated in an O_2-saturated 0.1 M Na_2SO_4 electrolyte using the rotating ring-disk electrode (RRDE) at 1,600 rpm. The polarization curves and corresponding ring current LSV curves shown in Fig. 4*A* exhibited significantly higher 2e ORR activity for InO_5S compared to InO_6 and InS_6. Within the broad potential window ranging from 0.35 V to 0.65 V (vs. RHE, Fig. 4 *B* and *C*), InO_5S displayed electron transfer numbers (n) below 2.30, with a minimum of 2.04 attained at 0.5 V (vs. RHE). Moreover, InO_5S exhibited a H_2O_2 selectivity exceeding 85.06%, reaching a maximum of 98.00%, which is significantly higher in comparison to InO_6 and InS_6. This observation is further confirmed by the FE (*SI Appendix*, Fig. S44). Notably, InO_5S demonstrated the highest partial current density for H_2O_2 production (j_{H2O2}) at 0.45 V, reaching –1.01 mA cm^{-2} (Fig. 4*D* and *SI Appendix*, Fig. S45), which was 1.12 and 1.43 times higher than that of InO_6 (–0.89 mA cm^{-2}) and InS_6 (0.70 mA cm^{-2}), respectively. Additionally, the kinetic current density (j_k, *SI Appendix*, Fig. S46) and Tafel slope (*SI Appendix*, Fig. S47) reveal the higher reaction kinetics of InO_5S compared to InO_6 and InS_6.

DFT calculations were performed to shed light onto the mechanism underlying the enhanced 2e ORR demonstrated by InO_5S. The adsorption energy of O_2 was found to be –0.89 eV (*SI Appendix*, Fig. S48) on InO_5S, significantly more favorable than that of InO_6 (–0.39 eV) and InS_6 (–0.08 eV), indicative of an increased O_2 affinity. The two-electron and four-electron pathways were then explored to unveil the propensity for O–O bond dissociation during the ORR process (*SI Appendix*, Figs. S49-S52). Interestingly, the two-electron pathways render negative reaction barriers (–0.34 eV for InO_6, –0.21 eV for InS_6 and –0.62 eV for InO_5S) and thus favorable, in stark contrast to four-electron pathways with positive reaction barriers (0.32 eV for InO_6, 0.40 eV for InS_6 and 0.31 eV for InO_5S, *SI Appendix*, Fig. S52). Moreover, the thermodynamic limiting potential (U_L) for the two-electron pathways was plotted as a function of ΔG_{*OOH}, whereby InO_5S exhibited a moderate ΔG_{*OOH} of 4.18 eV, corresponding to an U_L of 0.62 V for H_2O_2 formation (Fig. 4*E*). This value is closer to the theoretical U_L compared to InO_6 (0.34 eV) and InS_6 (0.21 eV), implying the superior 2e ORR selectivity of InO_5S. Additionally, the ICOHP results in Fig. 4*F* show that the strength of the In–O bond in InO_5S has an intermediate value of 3.43 eV, which is distinct from the stronger yet more undesirable In–O bonds in both InS_6 (4.53 eV) and InO_6 (4.67 eV). The COHP results (Fig. 4 *G* and *H*) further revealed that the higher occupancy of antibonding

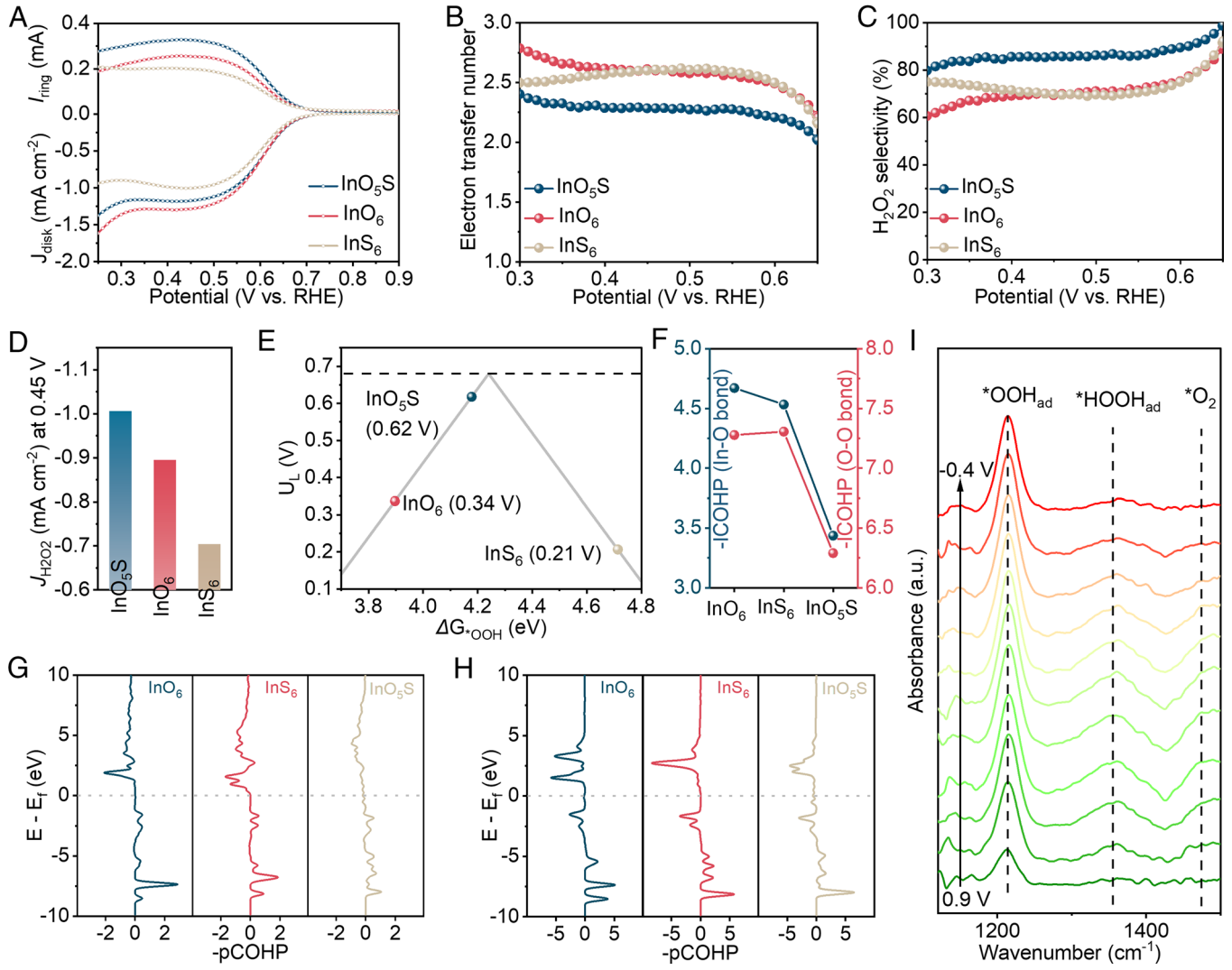

Fig. 4. Electrochemical 2e ORR performances of asymmetrically stretched InO_5S. (*A*) Disk polarization curves and corresponding ring currents at different electrode rotation speeds. Electron transfer numbers (*B*) and H_2O_2 selectivity (*C*) at different applied potentials. (*D*) j_{H2O2} at 0.45 V (vs. RHE). (*E*) Limiting potentials (U_L) as a function of ΔG_{*OOH} for InO_5S, InO_6, and InS_6. (*F*) Strength of the In–O and O–O bond as elucidated by –ICOHP. COHP for In–O (*G*) and O–O (*H*). (*I*) Electrochemical in situ FT-IR spectra for InO_5S.

orbitals in InS_6 and InO_6 resulted in stronger In–O and O–O bonds, which hindered subsequent hydrogenation and desorption of H_2O_2. In agreement, limited overlap of In and O orbitals was evidenced in the PDOS plot of InS_6 and InO_6 (*SI Appendix*, Fig. S53). Simultaneously, the strength of the O–O bond was found to be the weakest in InO_5S (6.29 eV), indicating the ease of further hydrogenation of the O–O bond and subsequent release of H_2O_2 in InO_5S.

In situ ATR-FTIR spectroscopy revealed the adsorption of the *OOH intermediate on InO_5S, as evidenced by the O–O stretching vibration at ~1,220 cm^{-1} (Fig. 4*I*), which progressively intensified with negative shifts in potential. Additionally, an absorption band attributed to adsorbed $*H_2O_2$ was detected around 1,350 cm^{-1}, further confirming the *OOH-mediated two-electron ORR pathway, for H_2O_2 production on InO_5S.

Electrocatalytic Performance of Trifunctional Electrosynthesis Systems for Small Molecules. Given that the asymmetrically stretched InO_5S catalyst yields excellent trifunctional activities for NORR, CO_2RR, and 2e ORR (Fig. 5*A*), the catalyst was coupled to the cathodic side in a flow-cell system to assess its multifaceted capabilities in producing small molecules, such as NH_3, formate, and H_2O_2. Traditional electrolysis systems are limited by their single-reactive-site nature, which constrains them to specific catalytic reactions (28–30), which hinders scalability and ability to adapt to the production of diverse small molecules, crucial for industrial applications and for generating primary and downstream chemical products. It is thus imperative to design an electrolysis system which supports diverse reactive sites. To meet this need, this study reports a flow-cell electrolysis system with InO_5S catalysts coated on a gas diffusion layer serving as the cathode (indicated in yellow), enabling the switching of catalytic reactions by merely changing the type of feed gas with multiple reactive sites (Fig. 5*B*). This approach eliminates the need to replace catalysts or dismantle the setup to swap to a different catalytic reaction, significantly lowering production costs and enhancing operational flexibility.

As shown in Fig. 5*C*, the electrolysis systems maintained stable and efficient NH_3 production in NORR with an average FE of 90.68% and NH_3 yield rate of 1353.36 μmoL h^{-1} cm^{-2} at a current density of 200 mA cm^{-2} over five continuous cycles (*SI Appendix*, Fig. S54). Afterward, by only replacing NO with CO_2 and O_2 as feed gases, the CO_2RR and 2e ORR performances were tested (in Fig. 5 *D* and *E* and *SI Appendix*, Figs. S55, S56). The CO_2RR and 2e ORR processes displayed a steady FE of 94.68% and 94.46% with a yield rate of 3.53 mmoL h^{-1} cm^{-2} for $HCOO^-$ and 3.52 mmoL h^{-1} cm^{-2} for H_2O_2 at a current density of 200 mA cm^{-2}, respectively. Compared to the best-reported catalysts, InO_5S also exhibits commendable H_2O_2 production activity (*SI Appendix*, Table S9). The consistency across all applied potentials indicates that InO_5S can act as an effective trifunctional cathode catalyst for the continuous electrosynthesis of various small molecules (NH_3, formate, and H_2O_2). Furthermore, upon alternating the production of small molecules through 2e ORR, NORR, and CO_2RR at a current density of 200 mA cm^{-2}, the voltage of catalysts quickly recovered and stabilized after each consecutive reaction test (Fig. 5*F*). The FEs (yield rate) (Fig. 5*G* and *SI Appendix*, Fig. S57, Table S10) observed in the three alternate tests for 2e ORR were 94.70 ± 0.63% (3.53 ± 0.02 mmoL h^{-1} cm^{-2}), 94.83 ± 1.07% (3.54 ± 0.04 mmoL h^{-1} cm^{-2}), and 95.40 ± 1.35% (3.53 ± 0.07 mmoL h^{-1} cm^{-2}); for NORR were 91.00 ± 0.46% (1.36 ± 0.01 mmoL h^{-1} cm^{-2}), 90.89 ± 1.28% (1.36 ± 0.02 mmoL h^{-1} cm^{-2}), and 91.53 ± 1.17% (1.37 ± 0.02 mmoL h^{-1} cm^{-2}); and for CO_2RR were 95.70 ± 1.63% (3.57 ± 0.06 mmoL h^{-1} cm^{-2}), 94.67 ± 1.79% (3.53 ± 0.07 mmoL h^{-1} cm^{-2}), and 95.59 ± 1.21% (3.57 ± 0.05 mmoL h^{-1} cm^{-2}), respectively. The collective results prove the stable and adaptable trifunctional small molecule electrosynthesis capabilities of our asymmetrically stretched InO_5S catalyst at high current densities, establishing it as a promising candidate for flexible and demand-driven electrosynthesis of small molecules.

Direct synthesis of Downstream Chemical Products using CO_2 and NO in Pure Water. Given the exceptional trifunctional activity (NORR, CO_2RR, and ORR) exhibited by the asymmetrically stretched InO_5S in cathodic reactions, it is well prepared for producing downstream chemical products. Compared to traditional liquid electrolytes like aqueous Na_2SO_4, solid electrolytes containing solid ion conductors facilitate the rapid transport of cations or anions. When combined with a highly selective InO_5S trifunctional catalyst, this setup can continuously produce high-purity downstream chemical products, avoiding the need for further separation from metal salts in the solvent (7, 31–33). Therefore, the asymmetrically stretched InO_5S catalyst was integrated into a full-cell device equipped with a solid electrolyte to produce pure solutions of downstream chemical products. In the full-cell system (Fig. 6*A*), cation exchange membranes (CEM) and anion exchange membranes (AEM) were strategically positioned at the anode and cathode sides of the solid electrolyte, respectively (7, 32). Their primary function was to act as barriers, isolating the anodic and cathodic electrolytes, while concurrently ensuring the efficient transfer of protons (H^+). On the cathodic side, the process involved the reduction of gases into negatively charged intermediates, which then combined with H^+ generated by the oxidation of H_2O at the anode, to form the primary products (such as NH_3, HCOOH, and H_2O_2). These products are collected as the sole liquid phase products of the corresponding reactions in deionized water, effectively avoiding the typically complex separation processes associated with multiple products and salt-containing electrolytes. As demonstrated in Fig. 6*A*, a series of parallel full-cell devices enabled the real-time mixing of NH_3 and HCOOH, products of NORR and CO_2RR, in deionized water to create an ammonium formate (NH_4COOH) solution (NH_3 + HCOOH → NH_4COOH) (34). This solution was then dried to produce solid NH_4COOH, a key downstream chemical product widely used in fuel cells and the chemical engineering industry (35–37). Additionally, the full-cell apparatus was capable of generating pure HCOOH and H_2O_2 via CO_2RR and ORR, respectively (Fig. 6*B*). In the presence of H_2SO_4, these compounds underwent a chemical reaction ($HCOOH + H_2O_2 \rightarrow HCOOOH + H_2O$), producing pure peroxyformic acid (HCOOOH) solution, which is a disinfectant suitable for on-demand production in the medical and food industries (38–40).

As a validation of this concept, shown in Fig. 6 *C* and *D*, in the parallel full-cell configuration (catalyst exposure area of 2 * 2 cm^2), NORR and CO_2RR were simultaneously executed at approximately 50 mA cm^{-2} and 20 mA cm^{-2}, respectively, for a duration of 10 h. The selection of these current densities was based on the theoretical matching of NH_3 and HCOOH production, which subsequently guided the adjustment of input voltages. After experimentation, the product was freeze-dried with deionized water, which formed a white powder product (1,167 mg, inset of Fig. 6*E*). XRD analysis confirmed that the crystal phase of this product, synthesized through the parallel full-cell system, matched that of standard NH_4COOH, with no additional peaks detected

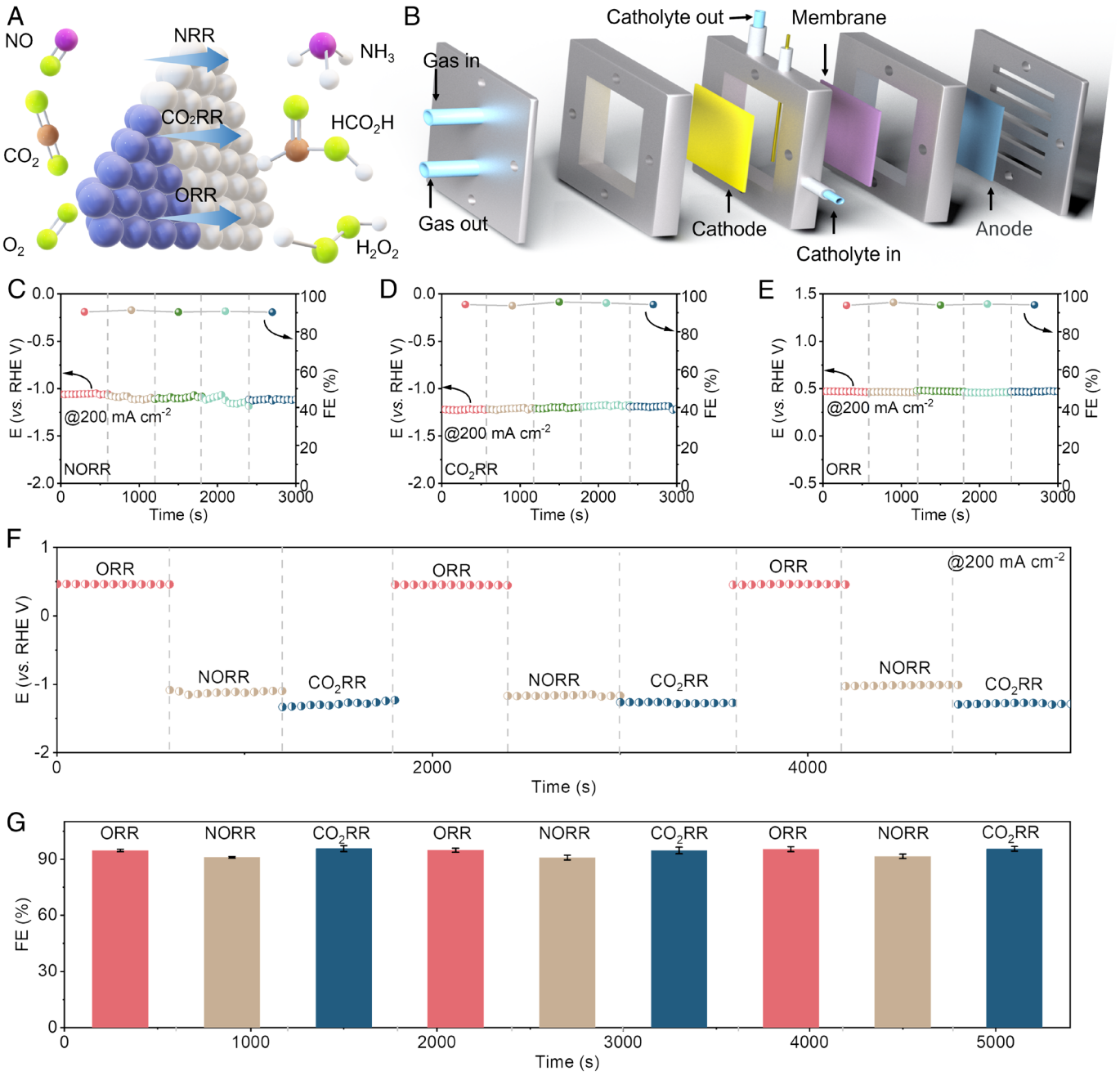

Fig. 5. Electrocatalytic performance of electrosynthesis systems for small molecules using asymmetrically stretched InO_5S as a trifunctional electrocatalyst. (*A*) Schematic diagram of the asymmetrically stretched InO_5S as a trifunctional electrocatalyst. (*B*) Schematic diagram of electrosynthesis system in flow-type cell configuration. Chronoamperometry curves and FEs of (*C*) NORR, (*D*) CO_2RR, and (*E*) 2e ORR for five cycles at 200 mA cm^{-2}. (*F*) Chronoamperometry curves of NORR, CO_2RR, and 2e ORR by alternating tests at 200 mA cm^{-2}. (*G*) Corresponding FEs of NORR, CO_2RR, and 2e ORR (experimental samples n = 3; Significance: $P < 0.05$, calculated using one-way ANOVA across different cycles).

(Fig. 6*E*). This finding was further substantiated by FT-IR spectra (Fig. 6*F*). These results unequivocally confirm the potential of using asymmetrically stretched InO_5S catalysts to produce pure NH_4COOH solid, utilizing CO_2, NO, and H_2O as sustainable raw materials.

Discussion

In summary, we have developed a parallel electrolysis device designed to transform greenhouse gases, including CO_2, NO, and other gases, into valuable downstream chemical products. The device features asymmetrically stretched InO_5S, crafted with symmetry-breaking In sites. Electrochemical results reveal that the symmetry-breaking In sites possess extraordinary multifunctional catalytic capabilities. Mechanistic studies revealed that the symmetry-breaking and redistribution of electronic structures result in a strong internal electric field, which significantly enhances the d-band center and adsorption of reaction intermediates, thereby promoting trifunctional catalytic activity. Consequently, when the catalyst was integrated into a flow electrolysis system, a sustained production of NH_3, $HCOO^-$, and H_2O_2 was observed, maintaining an FE above 90% at an industrial scale. The ability to switch catalytic reactions by solely changing the feed gas type and efficiently generating high-value chemicals like NH_4COOH demonstrates the versatility and efficiency of our system. This finding is pivotal as it addresses the challenges associated with the selective

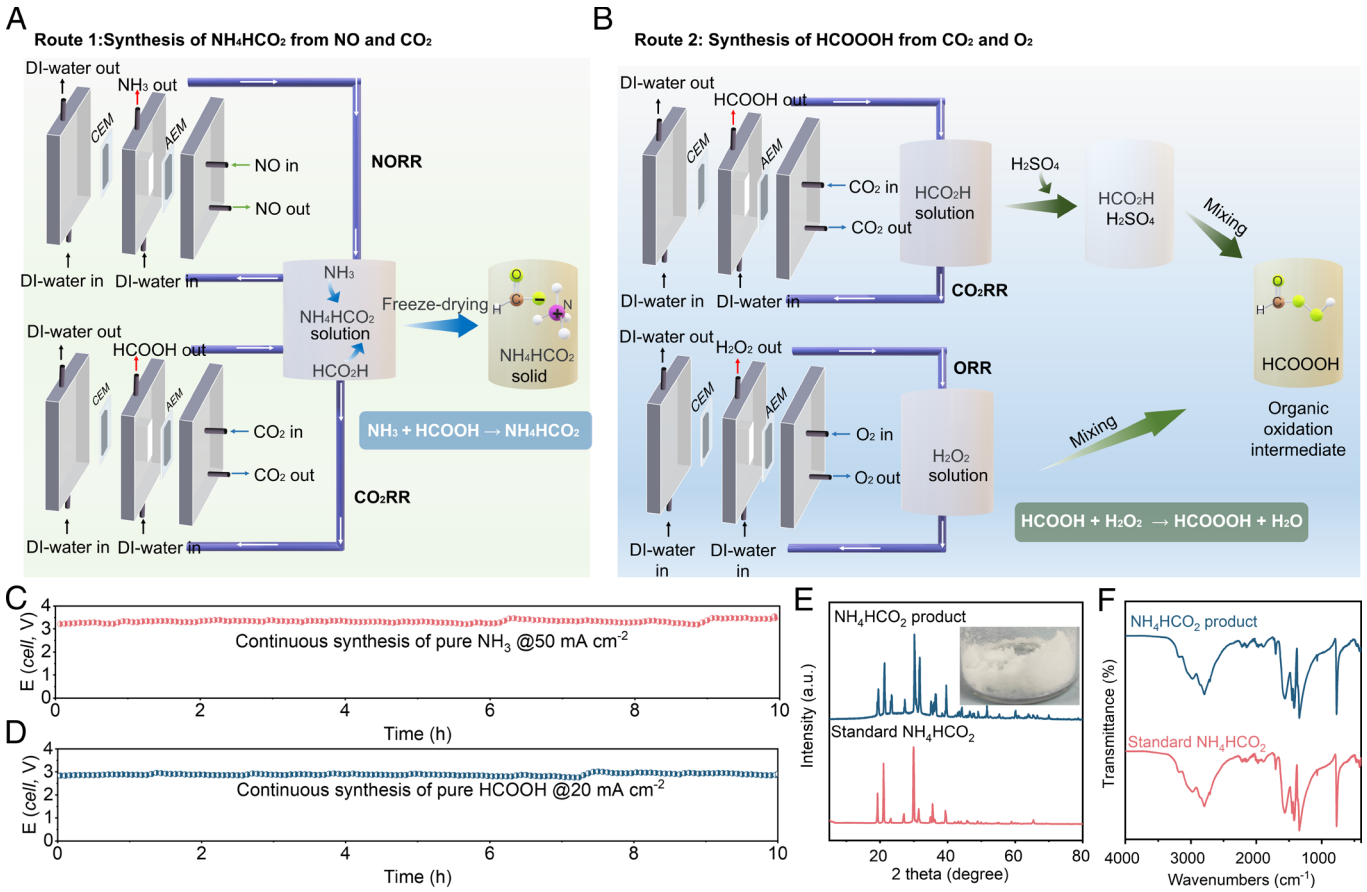

Fig. 6. Electrochemical direct synthesis of downstream chemical products using CO_2, NO, and O_2 in pure water by asymmetrically stretched InO_5S. (*A*) Schematic diagram of NH_4HCO_2 synthesized from NO and CO_2. (*B*) Schematic diagram of HCOOOH synthesized from CO_2 and O_2. Chronoamperometry curves of (*C*) NORR at 50 mA cm^{-2} for 10 h and (*D*) CO_2RR at 20 mA cm^{-2} for 10 h. (*E*) XRD pattern and (*F*) FT-IR spectrum of the NH_4HCO_2 product; the inset of (*E*) shows a digital image of the NH_4HCO_2 product.

conversion of multiple substrates within a single system, a significant improvement over traditional systems that typically require separate setups for each reaction type.

Although the results are promising, our study has several limitations: 1) While the device demonstrated high efficiency on a laboratory scale, scaling up the system for industrial applications presents challenges. 2) The potential for converting a wider range of gases remains significant but uncertain, necessitating further exploration. To address these limitations, future research should focus on the following key areas: 1) Utilizing advanced synthesis techniques and integrating machine learning algorithms to predict optimal catalyst compositions and structures at the atomic level. This approach can develop different catalysts with enhanced stability, activity, and selectivity. 2) Experimenting with different system designs and operating parameters can maximize efficiency, scalability, and long-term stability, which is crucial for transitioning from laboratory scale to pilot scale and eventually to industrial-scale operations. 3) Exploring the potential of other gas feedstocks, such as other greenhouse gases (e.g., methane and nitrous oxide), as raw materials for electrocatalytic conversion can expand the range of high-value products and further reduce greenhouse gas emissions.

Materials and Methods

Catalyst Preparation. Synthesis of indium metal-organic framework (In-MOF): A solution of 2-thiophenecarboxylic acid ($C_5H_4O_2S$, 2-TDC) was prepared by dissolving 100 mg of the compound in 10 mL of ethanol. This solution was then combined with a separate 20 mL ethanol solution containing 50 mg of $InCl_3{\cdot}4H_2O$ and 50 mg of $Zn(Ac)_2{\cdot}2H_2O$. The resulting mixture was heated at 120 °C for a duration of 12 h. The product was then collected and thoroughly washed with ethanol and water, respectively (average yield: 30.62 mg, *SI Appendix*, Table S1).

Synthesis of asymmetrically stretched InO_5S: The preobtained In-MOF powder (100 mg) was heated to 600 °C for 2 h at the heating rate of 5 °C min^{-1} under Ar atmosphere in a tube furnace and then naturally cooled to room temperature. The as-obtained products were then collected and washed with deionized water and dried in an oven at 60 °C (average yield: 58.68 mg, *SI Appendix*, Table S2).

Physical Characterization. Morphology was observed on a field emission scanning electron microscope (FESEM, JEOL 7800F), transmission electron microscope (TEM), and high-resolution transmission electron microscope (HRTEM, Titan G2 60-300, a spherical and chromatic aberration imaging corrector). Chemical composition was determined by inductively coupled plasma mass spectrometry (ICP-MS, Thermo XSERIES 2), energy-dispersive X-ray spectroscopy (EDS), and element mapping (150 to 230 Mx 200 kV on STEM). Crystal structure was examined by an X-ray diffractometer (XRD, D8 Advance, Bruker, Karlsruhe, Germany 9 kw, 40 kV, 40 mA, λ=1.5418 Å) with Cu-Kα radiation. Chemical state was analyzed by X-ray photoelectron spectroscopy (XPS) and ultraviolet photoelectron spectroscopy (UPS, Thermo ESCALAB 250XI between 0 and 1,400 eV). The passing energy used for XPS was 100 eV for survey scans, 20 eV for region scans, and 2 eV for UPS. Organic functional groups were recorded by Fourier transform infrared spectroscopy (FTIR spectra, Thermofisher NICOLETIS 10 FTIR spectrometer). Ultraviolet-visible (UV-vis) absorption spectra were recorded on Agilent Cary 60. 1 H NMR spectra were collected on a superconducting-magnet NMR spectrometer (Bruker AVANCE III HD 500 MHz).

In Situ Attenuated Total Reflectance–Fourier Transform Infrared (ATR-FTIR) Characterization. In situ ATR-FTIR spectra were performed using a Nicolet™ iS50 FT-IR spectrometer, equipped with a specialized reaction cell and a liquid nitrogen-cooled mercury cadmium telluride (MCT) detector. A 20 mm

diameter Au-coated Si hemispherical prism, sourced from MTI Corporation, served both as the conductive substrate for catalyst deposition and the IR reflection element. The electrochemical cell incorporated a Pt foil counter electrode, an Ag/AgCl (4 M KCl) reference electrode, and 0.1 M Na_2SO_4 as the electrolyte. Catalyst ink, with a loading density of 1 mg cm^{-2}, was formulated according to the same procedures used in prior electrochemical analyses. In situ ATR-FTIR spectra were acquired while sweeping the working electrode potential from OCP to the entire test range at a scan rate of 5 mV s^{-1}. The reaction chamber was continually flushed with ultrapure CO_2/NO/O_2 (99.999%), and spectral alterations were monitored. The spectral acquisition range spanned 4,000 to 1,000 cm^{-1}.

Electrochemical Characterizations.

Electrochemical NORR testing. A mixture of 5 mg of testing samples and 30 μL of 5 wt% Nafion solution was dispersed in 1 mL of isopropanol/DI-water (v/v = 4: 1) mixed solutions, which were ultrasonicated for 30 min to form a uniform catalyst ink. Next, 600 μL of the above catalyst ink was transferred to a 1.0 × 3.0 cm^2 gas diffusion layer (GDL), where the effective catalytic area is 0.5 × 2.0 cm^2 and mass loading is 1 mg cm^{-2}. Cathodic NORR was studied in a three-electrode H-type electrolytic cell under Ar- or NO-saturated conditions connected to a CHI 760E electrochemical workstation using the as-formed electrode as the working electrode, GDL as the counter electrode, Ag/AgCl/KCl (saturated) as the reference electrode, Nafion 115 membrane as the separator, 0.1 M Na_2SO_4 as electrolyte and 0.05 M H_2SO_4 aqueous solution as exhaust gas absorption chamber. The Ar or NO flow rate was kept at 20 mL min^{-1}. All the potentials measured in this study were referenced against reversible hydrogen electrode (RHE) according to the formula:

$$E_{RHE} = E_{Ag/AgCl} + 0.0592 \times pH + 0.197.$$

To analyze NORR activities, linear sweep voltammograms (LSVs) were performed at a scan rate of 5 mV s^{-1} in the potential range of −0.9 ~ 0 V (vs. RHE), and chronoamperometric test was carried out at different potentials for 1 h with continuous saturation Ar or NO flow in the electrochemical system. The electrolyte (extracted from the reaction cell and suitably diluted to bring the concentration within the range of the standard curve for ammonia) was sampled and analyzed when the reaction stabilized.

The testing of electrochemical CO_2RR and ORR performance is similar to that of NORR. For details, please refer to Supporting Information section.

Trifunctional electrocatalytic performance characterizations. Cathodic trifunctional electrocatalytic performance of the InO_5S electrode was tested in a three-electrode flow-type electrolytic cell under feed gas-saturated conditions connected to a CHI 760E electrochemical workstation. Other preparation methods are similar to the CO_2RR test methods. The cyclic stability of the electrocatalytic system was evaluated by sequentially conducting NORR, CO_2RR, and 2e ORR reactions five times at a current density of 200 mA cm^{-2}. After each test cycle, the electrolyte was analyzed for corresponding products, following specific analytical methods for each reaction. The flexibility of the electrocatalytic system was also assessed by alternately conducting NORR, CO_2RR, and 2e ORR reactions at a current density of 200 mA cm^{-2}. This method allowed us to rigorously evaluate the system's adaptability and stability under varying electrochemical conditions, demonstrating its capability to efficiently switch between different reactions while maintaining consistent performance.

DFT calculation details. Theoretical calculations were performed using the Vienna Ab initio Simulation Package code (41) based on the density functional theory. The Perdew–Burke–Ernzerhof functional (42) was employed for the exchange-correlation potential. Valence electron configurations of the pseudopotentials were adopted as 5 $s^2 5p^1$ for In, 2 $s^2 2p^4$ for O, 3 $s^2 3p^4$ for S, 2 $s^2 2p^2$ for C, and 1 s^1 for H. The vacuum thickness was set as 15 Å for InO_6, InS_6, and InO_5S models. The cutoff energy for plane wave was 500 eV and the energy convergence was 10^{-4} eV in both structural relaxation and self-consistent calculations. The Monkhorst–Pack K-point grids were 2 × 2 × 1, 2 × 2 × 1 and 2 × 1 × 1 for InO_6, InS_6, and InO_5S calculations, respectively. The entropy contribution and zero-point energy correction were taken into consideration to obtain the Gibbs free energy in all catalytic reaction calculations. The reaction species with the lowest Gibbs free energy was adopted for energy barrier and electronic structure calculations. Crystal orbital Hamilton population (43) was employed to investigate the chemical bonding and antibonding contributions to the band-structure energy. The charge density difference method was used for the revelation of electron transfer with visualization for electronic and structural analysis software (44).

The reaction pathway for NORR to NH_3 as follows:

$$NO + 5H^+ + 5e^- + * \rightarrow *NO + 5H^+ + 5e^-,$$

$$*NO + 5H^+ + 5e^- \rightarrow *NHO + 4H^+ + 4e^-,$$

$$*NHO + 4H^+ + 4e^- \rightarrow *NHOH + 3H^+ + 3e^-,$$

$$*NHOH + 3H^+ + 3e^- \rightarrow *NH_2OH + 2e^-,$$

$$*NH_2OH + 2H^+ + 2e^- \rightarrow *NH_2 + H_2O + H^+ + e^-,$$

$$*NH_2 + H_2O + H^+ + e^- \rightarrow *NH_3 + H_2O.$$

The reaction energy (ΔG) of each step was calculated by the free energy difference between the reactants and products after correction:

$$\Delta G = \Delta E + \Delta ZPE - T\Delta S,$$

where ΔE, ΔZPE, and $T\Delta S$ stand for the adsorption energy, the zero-point energy correction, and the entropy contribution, respectively. The free energy of species H^+ was calculated as that of 1/2 H_2.

Data, Materials, and Software Availability. All study data are included in the article and/or *SI Appendix*.

ACKNOWLEDGMENTS. This work is funded by the AcRF Tier 1 provided by the Ministry of Education (grant RG105/19) in Singapore, the National Natural Science Foundation of China (grants 52376193, 51888103, 92163124, and 12304084), and the Natural Science Foundation of Jiangsu Province (grants BK20220930 and BK20230097). We thank the staff of beamline BL13SSW at Shanghai Synchrotron Radiation Facility for their experimental support.

Author affiliations: [a]School of Chemistry, Chemical Engineering and Biotechnology, Nanyang Technological University, Singapore 637459, Singapore; [b]Key Laboratory for Soft Chemistry and Functional Materials, School of Chemistry and Chemical Engineering, School of Energy and Power Engineering, Nanjing University of Science and Technology, Nanjing 210094, China; [c]Environmental Chemistry and Materials Centre, Nanyang Environment & Water Research Institute, Interdisciplinary Graduate Programme, Nanyang Technological University, Singapore 637141, Singapore; and [d]Interdisciplinary Center for Fundamental and Frontier Sciences, Nanjing University of Science and Technology, Jiangyin, Jiangsu 214443, China

Author contributions: J.-M.L. and Y.S. designed research; Y.S. performed research; L.D., N.L.D.S., Y.L., M.T., J.D., S.C., and J.-M.L. analyzed data; and Y.S. and J.-M.L. wrote the paper.

The authors declare no competing interest.

1. Y. Yang *et al.*, Operando studies reveal active Cu nanograins for CO_2 electroreduction. *Nature* **614**, 262–269 (2023).
2. X. Tan, J. Nielsen, The integration of bio-catalysis and electrocatalysis to produce fuels and chemicals from carbon dioxide. *Chem. Soc. Rev.* **51**, 4763–4785 (2022).
3. Q. Dang *et al.*, Bias-free driven ion assisted photoelectrochemical system for sustainable wastewater treatment. *Nat. Commun.* **14**, 8413 (2023).
4. J. Gu, C.-S. Hsu, L. Bai, H. M. Chen, X. Hu, Atomically dispersed Fe^{3+} sites catalyze efficient CO_2 electroreduction to CO. *Science* **364**, 1091–1094 (2019).
5. J. Abdul Nasir *et al.*, Influence of solvent on selective catalytic reduction of nitrogen oxides with ammonia over Cu-CHA zeolite. *J. Am. Chem. Soc.* **145**, 247–259 (2023).
6. G.-F. Chen *et al.*, Electrochemical reduction of nitrate to ammonia via direct eight-electron transfer using a copper–molecular solid catalyst. *Nat. Energy* **5**, 605–613 (2020).
7. C. Xia, Y. Xia, P. Zhu, L. Fan, H. Wang, Direct electrosynthesis of pure aqueous H_2O_2 solutions up to 20% by weight using a solid electrolyte. *Science* **366**, 226–231 (2019).
8. T. Zheng *et al.*, Copper-catalysed exclusive CO_2 to pure formic acid conversion via single-atom alloying. *Nat. Nanotechnol.* **16**, 1386–1393 (2021).
9. B.-H. Lee *et al.*, Supramolecular tuning of supported metal phthalocyanine catalysts for hydrogen peroxide electrosynthesis. *Nat. Catal.* **6**, 234–243 (2023).
10. P. Zhu, H. Wang, High-purity and high-concentration liquid fuels through CO_2 electroreduction. *Nat. Catal.* **4**, 943–951 (2021).
11. J. Qi *et al.*, Energy-saving and product-oriented hydrogen peroxide electrosynthesis enabled by electrochemistry pairing and product engineering. *Nat. Commun.* **14**, 6263 (2023).
12. Y. S. Wu, Z. Jiang, Z. C. Lin, Y. Y. Liang, H. L. Wang, Direct electrosynthesis of methylamine from carbon dioxide and nitrate. *Nat Sustain* **4**, 725–730 (2021).

13. Y. Luo *et al.*, Selective electrochemical synthesis of urea from nitrate and CO_2 via relay catalysis on hybrid catalysts. *Nat. Catal.* **6**, 939–948 (2023).
14. C. Lv *et al.*, Selective electrocatalytic synthesis of urea with nitrate and carbon dioxide. *Nat Sustain* **4**, 868–876 (2021).
15. X. Wei *et al.*, Oxygen vacancy-mediated selective C-N coupling toward electrocatalytic urea synthesis. *J. Am. Chem. Soc.* **144**, 11530–11535 (2022).
16. J. Li, Y. Zhang, K. Kuruvinashetti, N. Kornienko, Construction of C–N bonds from small-molecule precursors through heterogeneous electrocatalysis. *Nat. Rev. Chem.* **6**, 303–319 (2022).
17. Z. Tao, C. L. Rooney, Y. Liang, H. Wang, Accessing organonitrogen compounds via C–N coupling in electrocatalytic CO_2 reduction. *J. Am. Chem. Soc.* **143**, 19630–19642 (2021).
18. R. Sun *et al.*, Heterogeneous catalysts for CO_2 hydrogenation to formic acid/formate: From nanoscale to single atom. *Energy Environ. Sci.* **14**, 1247–1285 (2021).
19. S. Zhao *et al.*, Deciphering nickel-catalyzed electrochemical ammonia synthesis from nitric oxide. *Chem* **9**, 3555–3572 (2023).
20. M. Dan *et al.*, Strategies and challenges on selective electrochemical hydrogen peroxide production: Catalyst and reaction medium design. *Chem Catal.* **2**, 1919–1960 (2022).
21. V. S. Saji, V. K. Pillai, *Multi-Functional Electrocatalysts: Fundamentals and Applications* (Royal Society of Chemistry, 2024).
22. B. Jia *et al.*, Indium cyanamide for industrial-grade CO_2 electroreduction to formic acid. *J. Am. Chem. Soc.* **145**, 14101–14111 (2023).
23. K. Chen, N. Zhang, F. Wang, J. Kang, K. Chu, Main-group indium single-atom catalysts for electrocatalytic NO reduction to NH_3. *J. Mater. Chem. A* **11**, 6814–6819 (2023).
24. E. Zhang *et al.*, Engineering the local atomic environments of indium single-atom catalysts for efficient electrochemical production of hydrogen peroxide. *Angew. Chem. Int. Ed.* **61**, e202117347 (2022).
25. Y. Zhou *et al.*, Asymmetric dinitrogen-coordinated nickel single-atomic sites for efficient CO_2 electroreduction. *Nat. Commun.* **14**, 3776 (2023).
26. Y. Sun *et al.*, Tuning coordination structures of Zn sites through symmetry-breaking accelerates electrocatalysis. *Adv. Mater.* **36**, e2306687 (2024).
27. J. Zhang *et al.*, Accelerating electrochemical CO_2 reduction to multi-carbon products via asymmetric intermediate binding at confined nanointerfaces. *Nat. Commun.* **14**, 1298 (2023).
28. H. L. Du *et al.*, Electroreduction of nitrogen with almost 100% current-to-ammonia efficiency. *Nature* **609**, 722–727 (2022).
29. C. Xia *et al.*, Confined local oxygen gas promotes electrochemical water oxidation to hydrogen peroxide. *Nat. Catal.* **3**, 125–134 (2020).
30. Y. Cao *et al.*, Surface hydroxide promotes CO_2 electrolysis to ethylene in acidic conditions. *Nat. Commun.* **14**, 2387 (2023).
31. C. Xia *et al.*, Continuous production of pure liquid fuel solutions via electrocatalytic CO2 reduction using solid-electrolyte devices. *Nat. Energy* **4**, 776–785 (2019).
32. Y. Xia *et al.*, Highly active and selective oxygen reduction to H_2O_2 on boron-doped carbon for high production rates. *Nat. Commun.* **12**, 4225 (2021).
33. X. Zhang *et al.*, Electrochemical oxygen reduction to hydrogen peroxide at practical rates in strong acidic media. *Nat. Commun.* **13**, 2880 (2022).
34. Z. J. Schiffer, S. Biswas, K. Manthiram, Ammonium formate as a safe, energy-dense electrochemical fuel ionic liquid. *ACS Energy Lett.* **7**, 3260–3267 (2022).
35. Z. Pan *et al.*, Development of a high-performance ammonium formate fuel cell. *ACS Energy Lett.* **8**, 3742–3749 (2023).
36. Q. H. Nguyen *et al.*, Development of simple analytical method for B-group vitamins in nutritional products: Enzymatic digestion and UPLC-MS/MS quantification. *J. Anal. Methods. Chem.* **2021**, 5526882 (2021).
37. I. Borthakur, S. Nandi, Y. Bilora, B. Sadhu, S. Kundu, Reductive aminomethylation using ammonium formate and methanol as N1 and C1 source: Direct synthesis of mono- and di-methylated amines. *ACS Catal.* **14**, 5847–5857 (2024).
38. J. Bu, Y.-T. Wang, M.-C. Deng, M.-J. Zhu, Enhanced enzymatic hydrolysis and hydrogen production of sugarcane bagasse pretreated by peroxyformic acid. *Bioresour. Technol.* **326**, 124751 (2021).
39. F. Sanger, Oxidation of insulin by performic acid. *Nature* **160**, 295–296 (1947).
40. R. Gehr, D. Chen, M. Moreau, Performic acid (PFA): Tests on an advanced primary effluent show promising disinfection performance. *Water Sci. Technol.* **59**, 89–96 (2009).
41. G. Kresse, J. Furthmiiller, Efficient iterative schemes for ab initio total-energy calculations using a plane-wave basis set. *Phys. Rev. B* **54**, 11169–11186 (1996).
42. J. P. Perdew, K. Burke, M. Ernzerhof, Generalized gradient approximation made simple. *Phys. Rev. Lett.* **77**, 3865–3868 (1996).
43. R. Dronskowski, P. E. Blöchl, Crystal orbital hamilton populations (COHP). energy-resolved visualization of chemical bonding in solids based on density-functional calculations. *J. Phys. Chem.* **97**, 8624–9617 (1993).
44. K. Momma, F. Izumi, VESTA 3 for three-dimensional visualization of crystal, volumetric and morphology data. *J. Appl. Crystallogr.* **44**, 1272–1276 (2011).